

Article

Effects of Acetone Vapor on the Exciton Band Photoluminescence Emission from Single- and Few-Layer WS₂ on Template-Stripped Gold

Samantha Matthews ¹, Chuan Zhao ², Hao Zeng ² and Frank V. Bright ^{1,*}

¹ Department of Chemistry, Natural Sciences Complex, University at Buffalo, The State University of New York, Buffalo, NY 14260-3000, USA; smatthew@buffalo.edu

² Department of Physics, Fronczak Hall, University at Buffalo, The State University of New York, Buffalo, NY 14260-3000, USA; chuanzha@buffalo.edu (C.Z.); haozeng@buffalo.edu (H.Z.)

* Correspondence: chefvb@buffalo.edu; Tel.: +1-716-645-4180; Fax: +1-716-645-6963

Received: 13 March 2019; Accepted: 18 April 2019; Published: 23 April 2019



Abstract: Two-dimensional (2D) materials are being used widely for chemical sensing applications due to their large surface-to-volume ratio and photoluminescence (PL) emission and emission exciton band tunability. To better understand how the analyte affects the PL response for a model 2D platform, we used atomic force microscopy (AFM) and co-localized photoluminescence (PL) and Raman mapping to characterize tungsten disulfide (WS₂) flakes on template-stripped gold (TSG) under acetone challenge. We determined the PL-based response from single- and few-layer WS₂ arises from three excitons (neutral, A⁰; biexciton, AA; and the trion, A⁻). The A⁰ exciton PL emission is the most strongly quenched by acetone whereas the A⁻ PL emission exhibits an enhancement. We find the PL behavior is also WS₂ layer number dependent.

Keywords: single- and few-layer WS₂; atomic force microscopy; Raman and Photoluminescence mapping; vapor sensing

1. Introduction

Transition metal dichalcogenides (TMDs), such as MX₂, where M = Mo or W (but can be most transition metals from groups IV, V, VI, and VIII), and X = Se, S, or Te, consist of one metal atomic layer hexagonally packed between two chalcogenide atomic layers [1–6]. The metal possesses six-fold in-plane coordination and the chalcogenide layers can be trigonal or octahedral [1,2]. In the trigonal prismatic (2H) form, the TMD will be semiconducting; and in the octahedral form (1T), the TMD is metallic [3,6]. In either phase, the bond between the metal and chalcogen atom is covalent, and the layers are held together by weak van der Waals forces [4].

Transition metal dichalcogenides have been studied for many years because the bulk materials exhibit an indirect bandgap whereas their single-layer counterparts possess a direct bandgap [1–5]. Early thin layer TMD research focused on creating new, two-dimensional (2D) field-effect transistors (FETs), nanoelectronics, photo detectors, and sensors [7–12]. For example, conductance-/resistance-based measurements have been performed on single- and few-layer MoS₂ to detect NO₂, NH₃, humidity, trimethylamine, acetone, and dichloromethane [9,10]. Resistance-based measurements using WS₂ thin films at 150 °C, exhibit sensitivity to H₂, NH₃, and NO₂ [12]. Similarly, Huo et al. [11] reported O₂, air, EtOH, and NH₃ sensing by using single- and few-layer WS₂ as photo detectors. Theoretical first-principles studies [13,14] have suggested that adsorbed NO, O₂, H₂O, and CO molecules on single- and few-layer WS₂ can change the WS₂ electronic and optical properties, making WS₂ an attractive candidate for room temperature gas sensing platforms. In

addition, Cho et al. [15] used photoluminescence (PL)-based measurements on single- and few-layer MoS₂ to detect NO₂ and NH₃. To the best of our knowledge, there has yet to be any report exploiting the PL emission from single- and few-layer WS₂ for chemical sensing. We have chosen WS₂ as our model TMD because the PL emission from single-layer WS₂ is 20 to 40 times more intense in comparison to single-layer MoS₂ [16], and, where the PL gradually decreases with increasing film thickness in WS₂, there is a drastic decrease from single- to bi-layer MoS₂ [17].

WS₂ has three main Raman active phonon modes (2LA(M), ~350 cm⁻¹; E¹_{2g}, ~355 cm⁻¹; and A_{1g}, ~418 cm⁻¹) [2,4]. The difference in energy between the E¹_{2g} and A_{1g} bands (Δ) and the 2LA/A_{1g} intensity ratio depends on the number of WS₂ layers [2]. Single- and few-layer WS₂ also exhibits a strong PL emission and the emission spectrum arises from three excitons [4,18], including the neutral exciton (A⁰, an electron and hole bound together), biexciton (AA, two neutral excitons bound weakly), and trion (A⁻, two electrons and one hole). Previous single point PL emission experiments [15] on single-layer MoS₂ specimens have shown that the A⁰ and A⁻ exciton bands behave differently when different gaseous vapors pass over the 2D specimen. For example, NO₂ (electron acceptor)/NH₃ (electron donor) vapors cause the A⁻ band amplitude to increase/decrease whereas the A⁰ band amplitude to decrease/increase [15].

Although most research has studied WS₂ on SiO₂/Si substrates, we chose gold substrates because of their applications in tip-enhanced Raman scattering (TERS) spectroscopy to enhance the Raman and PL signal and allow improved spatial resolution and scanning Kelvin probe microscopy (SKPM), to study the specimen's electronic properties.

In this paper, we determine the acetone-induced changes in the A⁰, AA, and A⁻ exciton band amplitude, peak energy, and energy distribution across individual WS₂ flakes that consist of single- and few-layer regions by using co-localized, confocal Raman, and PL emission mapping experiments.

2. Materials and Methods

2.1. WS₂ Materials and Supplies

The following were used: Acetone (Fisher Scientific, Hampton, NH, USA); Ar gas (Jackson Welding&Gas Products, Buffalo, NY, USA); N₂ gas (Airgas, Randor, PA, USA); polymethyl methacrylate (PMMA) (MW 120K, Sigma Aldrich, St. Louis, MO, USA); sulfur ($\geq 99.95\%$ purity, Alfa Aesar, Haverhill, MA, USA); tetrahydrofuran (THF, HPLC grade (Pharmco-Aaper, Brookfield, USA)); WO₃ (99.98% purity, Acros Organics, VWR, Randor, PA, USA); Au evaporation pellets (Kurt J. Lesker Co., Jefferson Hills, PA, USA); Epo-Tek 377 epoxy (Epoxy Technology, Billerica, MA, USA); p-type, boron-doped silicon wafers (<100>) (650 to 690 μm thickness and 1 to 10 $\Omega\text{-cm}$ resistivity, Alsil Supply Division Ymart, Palm Beach Gardens, FL, USA); and sapphire substrates (Hefei Keijing Materials Technology, Hefei, China).

2.2. 2D WS₂ Fabrication

Ultrathin WO₃ films were deposited by electron beam evaporation onto sapphire substrates by using an ATC Series UHV dual chamber deposition system. These films, along with S were placed in consecutive zones inside a quartz furnace tube. A simplified diagram depicting the fabrication scheme [19] can be found in the Supplementary Materials in Figure S3. Zone 1 contained ~4 to 8 mg of S and was placed 30 cm upstream from zone 2, which held the WO₃ film. Both zones had independently controlled temperatures, and the temperature ramping profiles were used to control the S vapor pressure at the WS₂ growth temperature. The carrier gas was N₂ with a flow rate of 40 standard cubic centimeters per minute (sccm) at ambient pressure. The zone 1 source temperature (containing S) was increased to 190 °C at a rate of 6 °C/min, and heating of this zone was stopped after 5 min. The temperature in zone 2 was increased at the same time as zone 1 to 745 °C at a rate of 25 °C/min. The temperature was then kept at 745 °C for 5 min to allow WS₂ growth. After the 5 min growth time,

the heaters and N₂ flow were turned off to obtain single layer WS₂ with some few layer overgrowth. A proposed WS₂ from the WO₃ mechanism has been described elsewhere [19,20].

2.3. Template Stripped Gold (TSG) Fabrication

Template stripped gold was created in several steps [21]. Initially, 125 nm of Au was deposited onto an Si wafer by e-beam evaporation (AXXIS electron-beam evaporator with glancing angle deposition (Kurt J. Lesker Co.). This Au-coated wafer was cut into roughly 1 cm × 1 cm squares by using a diamond tip cutter. A second Si wafer, without Au coating, was cut into roughly 1.5 cm × 1.5 cm squares by using a diamond tipped cutter. A drop of epoxy was placed on the Au-coated Si wafer and the uncoated Si wafer was placed on top of this, effectively sandwiching the Au. The sample was then cured in an oven at 150 °C for 1 h. After cooling, the epoxy “sandwich” was placed in a beaker of THF for 1 h to facilitate the separation between the Au and the Si wafer it was deposited on. The resulting substrate was an ultra-flat Au surface with an RMS (root mean square) roughness of ~0.7 nm.

2.4. WS₂ Exfoliation onto TSG

WS₂ samples were exfoliated onto TSG films by using the “water droplet method” [22]. Briefly, PMMA (1.2 M) was dissolved in chlorobenzene and spin coated onto the WS₂ flakes prepared atop a sapphire substrate. After 5 min at 80 °C, a water droplet was placed on top of the PMMA layer and the PMMA edge was poked with a sharp tweezer to allow water to penetrate underneath the WS₂ layer; this resulted in WS₂-sapphire separation. The resulting PMMA-WS₂ film was then transferred onto the TSG and heated for 10 min at 80 °C to remove water. The PMMA was then dissolved away by using acetone.

2.5. Raman, AFM, and PL Instrumentation

All Raman and PL measurements were performed by using a LabRam HR (Horiba, Edison, NJ, USA) with a 100× objective (LM Plan FL N, NA = 0.80, Olympus, Center Valley, PA, USA). The excitation source was a 532.06 nm laser (Laser Quantum, Fremont, CA, USA). Detection was performed by using a one-electrode thermoelectrically cooled CCD detector (Andor Technology Inc., Belfast, Northern Ireland). The entire system was controlled by LabSpec 6 software (Horiba).

Atomic force microscopy (AFM) measurements were recorded by using an AIST-NT model SmartSPM 1000 in intermittent contact mode with an Al-coated Si probe (k = 2 N/m, 240 μm length) (AC240TM-R3, Oxford Instruments Asylum Research, Santa Barbara, CA, USA) operating at a 70 kHz resonant frequency and controlled by Omega software 3.5.81 (AIST-NT).

2.6. AFM and Raman Studies

Atomic force microscopy height and phase images were recorded from 10 μm × 10 μm areas at a 512 × 512-pixel resolution (ca., 19.5 nm/step). Co-localized Raman and PL emission maps were acquired from 10 μm × 10 μm areas at a 64 × 64-pixel resolution (ca., 156 nm/step). All Raman and PL experiments were performed by using 600 and 300 grooves/mm gratings, respectively, yielding 1.6 cm⁻¹ and 3.1 nm spectral resolutions, respectively. The incident laser power density for all Raman and PL experiments was 510 W/cm² and 130 W/cm², respectively. All image and maps were recorded at 1.0 Hz/pixel.

2.7. Gaseous Analyte Vapor Studies

The WS₂ specimens were placed within a custom-built Teflon flow cell with a glass optical port. The flow cell was maintained at room temperature (294–296 K) while the WS₂ specimen was subjected to air or acetone vapor environments. The air/acetone cycle was performed at least three times on the same specimen to determine reproducibility (no detectable hysteresis). At least three specimens were assessed. Typical results are shown.

3. Results and Discussion

3.1. Layer Thickness Determination

Figure 1a presents typical AFM height (left) and phase (right) images from a WS₂ flake on TSG. The WS₂ appears to be wrinkled and ridges in the height image correspond to areas with low phase values (e.g., -20°) whereas regions that appear less wrinkled have more uniform, higher phase values (e.g., $+10^\circ$). Phase imaging in AFM is a measure of the energy dissipation between the AFM probe tip and the sample. This depends on many factors, including specimen-to-substrate adhesion [23] (pp. 69–71). In our case, a lower phase value indicates lower adhesion between regions within the WS₂ flake and the Au substrate while higher phase values indicate greater adhesion between regions within the WS₂ flake area and the Au substrate. The results shown in Figure 1a are consistent with WS₂ flakes that are wrinkled on the TSG surface where the WS₂ ridges are in poor contact with the Au substrate.

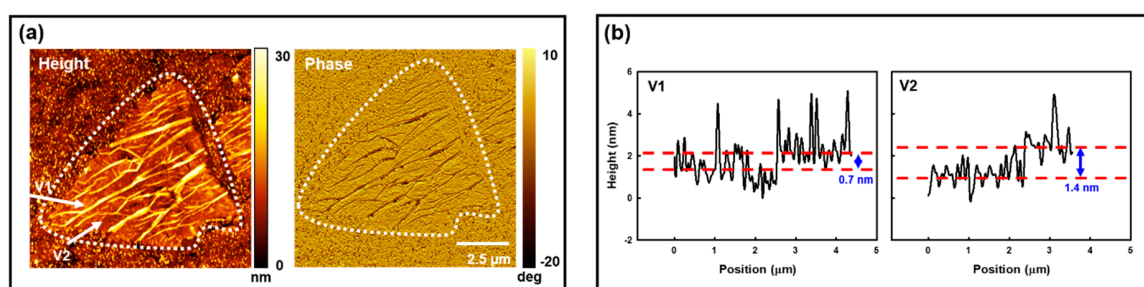


Figure 1. Typical AFM results for a WS₂ flake on TSG. (a) Typical AFM height (left) and phase (right) images. The dotted curve is used to outline the WS₂ flake. Two vectors (V1 and V2) are shown in the height image. (b) Typical height profiles along the V1 (left) and V2 (right) vectors shown in panel a. The V1 and V2 vectors traverse largely single- and two-layer regions, respectively.

In Figure 1b, we present AFM height profiles along the two vectors shown in Figure 1a (left). The V1 vector traverses a pathway that is largely single-layer WS₂ and the V2 vector follows a path that appears to be largely composed of two-layer WS₂. Unfortunately, the WS₂ wrinkles make it very challenging to assess our WS₂ flake thickness by using AFM alone.

Figure 2 presents typical diffraction limited, single-point Raman spectra recorded at WS₂ flake edges devoid of wrinkles that were determined by AFM height measurements to be either single- (Figure 2a) or few-layer (Figure 2b). All detectable Raman bands are labeled [2], including the key 2LA, E¹_{2g}, and A_{1g} bands. Using the known AFM-derived height at specific locations across a WS₂ flake, the boxed insets in Figure 2a,b show that the I_{2LA}/I_{A1g} and Δ (difference in the 2LA-A_{1g} band maxima) are layer number dependent and can be readily used to distinguish single- and few-layer WS₂ even on a heavily wrinkled specimen.

Figure 3 presents typical Raman-based mapping results from an isolated WS₂ flake on TSG. Figure 3a,b illustrate the I_{2LA}/I_{A1g} - and Δ -based maps, respectively (the original 2LA and A_{1g} intensity and position maps can be found in the Supplementary Materials in Figures S1 and S2). Figure 3c presents a layer count map created by multiplying Figure 3a,b. An inspection of these data shows that this particular WS₂ flake has a center region that consists of few-layer (mostly two-layer) WS₂ and the flake remainder is composed, largely, of single-layer WS₂.

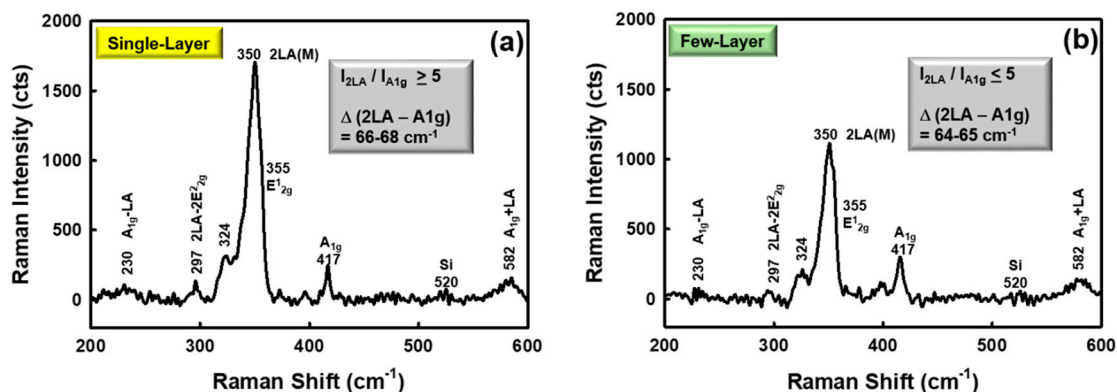


Figure 2. Typical single point Raman spectra and band assignments for different areas on a WS₂ flake on TSG. (a) Single-layer region. (b) Few-layer region.

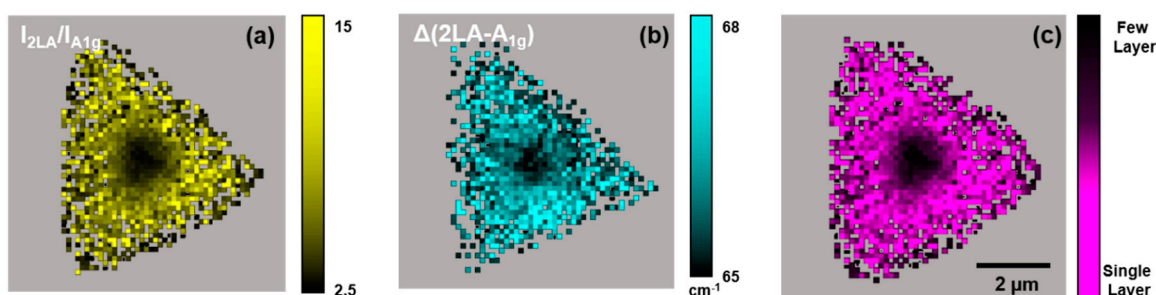


Figure 3. Typical WS₂ layer count maps for a single WS₂ flake on TSG. (a) I_{2LA}/I_{A1g} intensity ratio map. (b) $\Delta(E_{2LA} - E_{A1g})$ band energy difference map. (c) Combined a and b WS₂ layer count map.

3.2. Acetone Effect on WS₂ Flake Total PL and Exciton Band Emission

Figure 4 presents typical total PL emission intensity (1.8–2.1 eV) maps for the WS₂ flake shown in Figure 3 under air (Figure 4a) or acetone vapor atmospheres (Figure 4b). Two specific locations on this WS₂ flake are labeled in Figure 4a, denoting regions that are composed of single- (black circle) and few-layer (white circle) WS₂. These locations were selected based on the material classification scheme shown in Figure 3. Figure 4c presents the PL intensity ratio ($PL_{Air}/PL_{Acetone}$) map from the data in Figure 4a,b. An inspection of these data shows that the PL emission intensity: (i) Is heterogeneous across the WS₂ flake when it is under air or acetone vapor, (ii) is generally quenched by acetone vapor, and (iii) quenching is heterogeneous across the WS₂ flake. The largest extent of PL quenching is observed at the flake's middle and upper and lower edges, where the flake is mostly composed of few-layer WS₂ (cf., Figure 3). Thus, there is a strong spatial dependence in the acetone-induced PL emission quenching from a WS₂ flake.

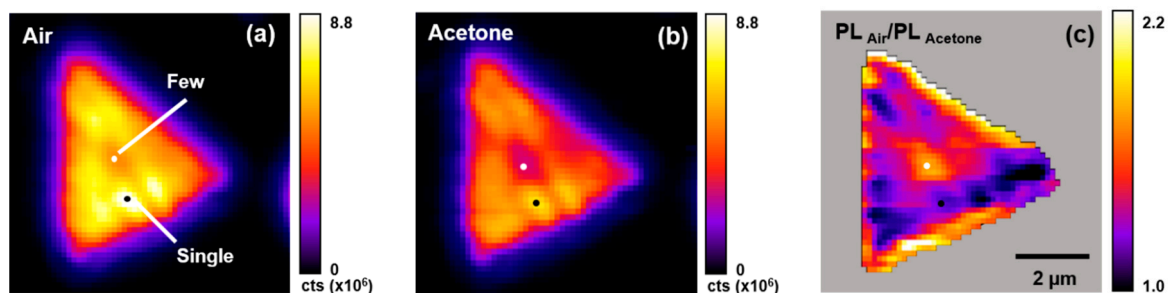


Figure 4. Typical total PL emission intensity maps (1.8–2.1 eV) for a single WS₂ flake on TSG. (a) Air atmosphere. (b) Acetone atmosphere. (c) $PL_{Air}/PL_{Acetone}$ intensity response map. The black and white dots indicate single- and few-layer WS₂ regions determined from Figure 3c.

Figure 5 present typical diffraction limited, single-point PL emission spectra from the WS₂ specimen shown in Figure 3 measured at locations within the flake (cf., Figure 3c) that are composed of single- (Figure 5a) or few-layer (Figure 5b) WS₂. Within each panel series are spectra recorded in air (1) and under acetone vapor (2) plus the corresponding PL emission energy-dependent $PL_{Air}/PL_{Acetone}$ response spectra (3). The dashed line in spectra 3 (located at 1.0) denotes where there is no detectable PL emission quenching. Energy regions with $PL_{Air}/PL_{Acetone}$ values < 1 exhibit acetone-induced PL enhancement whereas energy regions with $PL_{Air}/PL_{Acetone}$ values > 1 exhibit acetone-induced PL quenching. The PL emission spectra labeled 1 and 2 were individually curve fitted to models having two or three exciton emission bands (Gaussian). The best fit ($r^2 > 0.99$) was observed for a three band model and is consistent with emission from the A⁰, AA, and A⁻ excitons as reported by other researchers [4,18,24]. The general assignment of each WS₂ exciton band in the current research is based on previous reports in the literature [4,16,18,24]. We have also noticed that the AA exciton band exhibits a laser power-dependent position shift and a non-linear increase in amplitude with increasing laser power (results not shown). This behavior is consistent with an AA exciton being present [16]. Together, these data show that there are dramatic differences in the A⁰, AA, and A⁻ exciton emission susceptibility and response to acetone vapors and also a strong WS₂ layer number dependency. This has significant ramifications in the construction of PL-based sensors using such a platform and illustrates several potential opportunities for the creation of a tailored sensor response. For example, in quenchometric sensors [25,26], the quencher (Q) causes the PL emission intensity (PL) to decrease in a Q-dependent manner [25,26]. A response curve is created by plotting $PL_0/PL_{analyte}$ vs. $[Q]$, where PL_0 and $PL_{analyte}$ represent the PL emission intensities in the absence and presence of Q, respectively. An ideal quenchometric sensor exhibits a response curve with high sensitivity (i.e., $d((PL_0/PL_{analyte})/d[Q])$ [25,26].

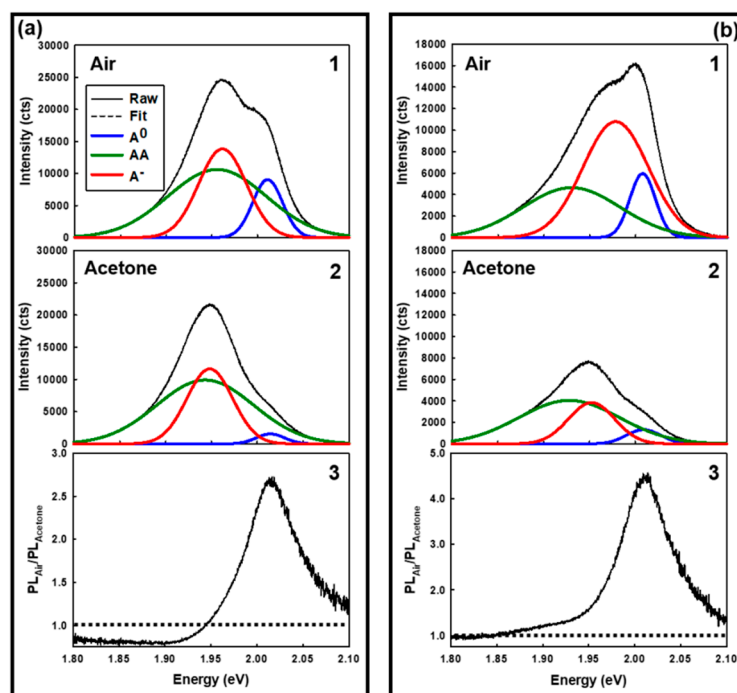


Figure 5. Typical single point PL emission spectra and curve fits from specific locations on the WS₂ flake shown in Figure 4. (a) Spectra from a single-layer WS₂ region. (b) Spectra from a few-layer WS₂ region. (1) Spectra recorded in air. (2) Spectra recorded under acetone vapor. (3) Energy-dependent $PL_{Air}/PL_{Acetone}$ response spectra. The dashed line in spectra 3 located at 1.0 denotes no quenching. Spectral regions with $PL_{Air}/PL_{Acetone} < 1$ exhibit a PL enhancement under acetone vapor. Spectral regions with $PL_{Air}/PL_{Acetone} > 1$ exhibit a PL quench under acetone vapor.

Figures 6–8 present typical A^0 , AA, and A^- PL emission exciton band amplitude, band maxima (eV), and band full width at half maximum (FWHM) (eV) maps, respectively, for the WS_2 flake shown in Figures 3 and 4. These air- and acetone-dependent exciton species maps were created by curve fitting the individual PL emission spectra in air and under acetone vapor at each pixel within the region of interest (4096 separate spectra) as described in Figure 5.

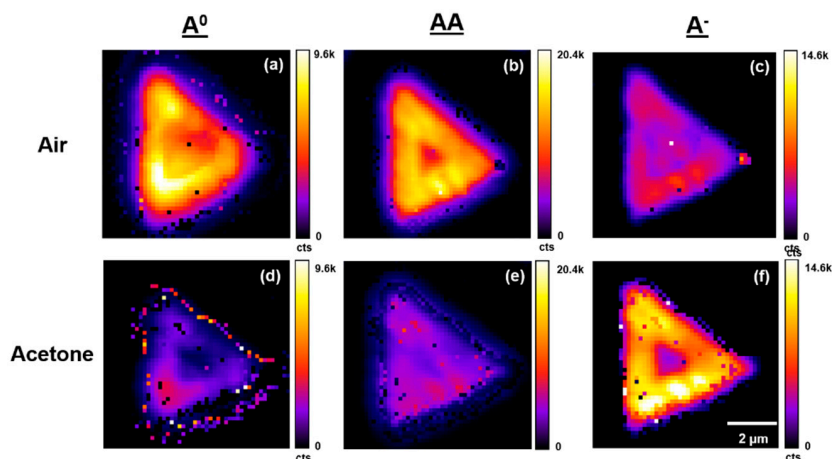


Figure 6. Typical PL emission A^0 , AA, and A^- exciton band amplitude maps for a single WS_2 flake on TSG under air and acetone vapors. Maps are generated by curve fitting PL emission spectra at each pixel across the entire flake. (a,b,c) Maps in air. (d,e,f) Maps under acetone vapor.

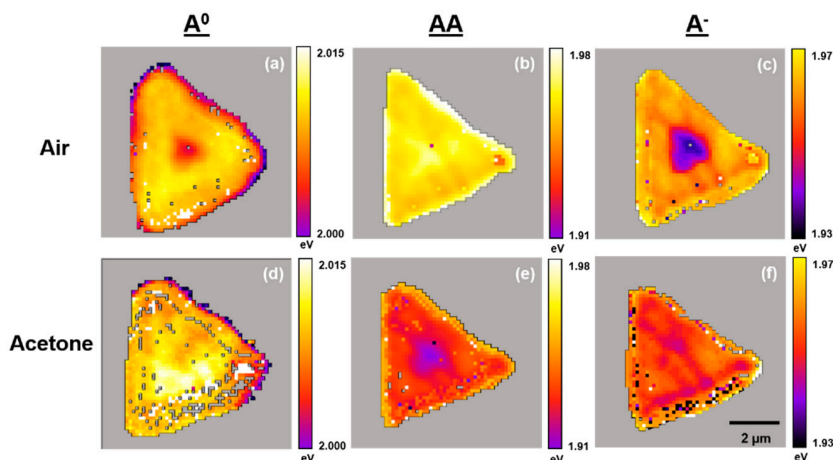


Figure 7. Typical PL emission A^0 , AA, and A^- exciton band maxima (eV) maps for a single WS_2 flake on TSG under air and acetone vapors. Maps are generated by curve fitting PL emission spectra at each pixel across the entire flake. (a,b,c) Maps in air. (d,e,f) Maps under acetone vapor.

Figure 9 summarizes the impact of acetone vapor on the A^0 , AA, and A^- exciton emission bands from an individual WS_2 flake on TSG. Several aspects of these results merit further discussion. In a general sense, the response depends on the emission exciton type and WS_2 layer number. The A^0 exciton from single-layer WS_2 exhibits the highest acetone-induced quenching sensitivity ($PL_{Air}/PL_{Acetone}$ up to 20). The A^0 exciton from few-layer WS_2 exhibits an acetone-induced quenching sensitivity that is generally 1/4 the corresponding single-layer value. The AA exciton from single-layer WS_2 is only 1/3 as sensitive ($PL_{Air}/PL_{Acetone}$ up to 7) to acetone-induced quenching in comparison to the single-layer A^0 exciton. The AA exciton from few-layer WS_2 is not particularly sensitive to acetone-induced quenching ($1.0 \geq PL_{Air}/PL_{Acetone} \geq 1.5$). The A^- exciton exhibits unique PL emission behaviors. The A^- exciton from few-layer WS_2 exhibits only modest acetone-induced quenching sensitivity ($1.1 \geq PL_{Air}/PL_{Acetone} \leq 1.5$). Interestingly, the A^- exciton band from the lion's share of single-layer WS_2 is the only band within

the flake to exhibit an acetone-induced PL emission enhancement ($0.1 > PL_{Air}/PL_{Acetone} \leq 0.5$). It is well known that acetone acts as an electron donor in the presence of MoS₂ and WS₂ [9,15,27,28]. A previous study on MoS₂ [15] shows that the positive trion (one electron, two holes, A⁺) band amplitude decreases in the presence of an electron donor, and the authors reasoned that when additional electrons are introduced from an electron donor, the PL spectrum is suppressed because of dissociation of the positive trions from the neutral excitons (A⁰). We determine the enhancement seen in our results is from the negative trion (two electrons, one hole, A⁻) accepting additional electrons from the electron donor, which results in an increase in the PL spectrum for the A⁻.

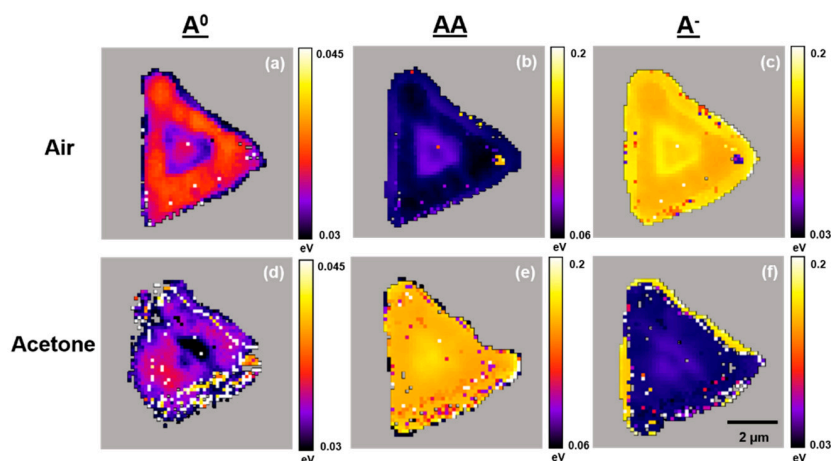


Figure 8. Typical PL emission A⁰, AA, and A⁻ exciton band FWHM (eV) maps for a WS₂ flake on TSG under air and acetone vapors. Maps are generated by curve fitting PL emission spectra at each pixel across the entire flake. (a,b,c) Maps in air. (d,e,f) Maps under acetone vapor.

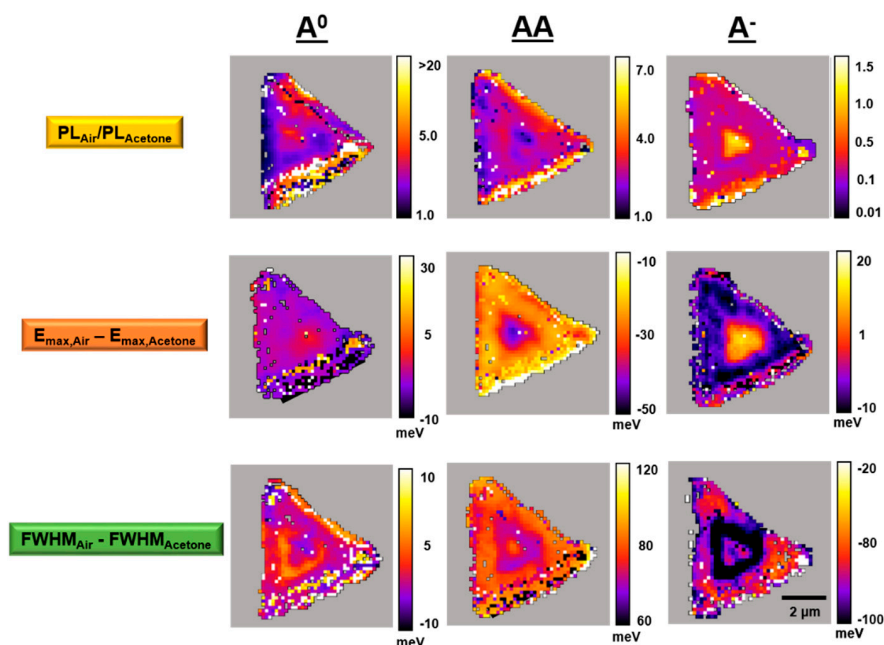


Figure 9. Typical acetone vapor-dependent PL emission A⁰, AA, and A⁻ exciton band intensity ratio ($PL_{Air}/PL_{Acetone}$), band energy maxima difference ($E_{max,Air} - E_{max,Acetone}$), and band FWHM energy difference ($FWHM_{Air} - FWHM_{Acetone}$) maps for a single WS₂ flake on TSG.

Acetone also induces detectable shifts in the exciton emission band energies. The energy shifts in the A⁰ exciton emission band across the WS₂ flake are the least distinct, but there are up to +30 meV shifts from regions that also exhibit the highest acetone susceptibilities (single-layer WS₂). The energy

shifts within the few-layer region are very small (just +5 meV) for the A^0 exciton emission band. The energy shifts in the AA exciton emission band across the WS_2 flake produces a very distinct pattern. In the single-layer region, the acetone-induced shift is up to -10 meV. In the few-layer region, the corresponding shift is up to -50 meV. This could arise from the topmost WS_2 layer within the few-layer region. The energy shifts in the A^- exciton band emission across the WS_2 flake produces another distinct pattern. In the single-layer region, the acetone-induced shift is small (0 to +10 meV). In the few-layer region, the corresponding shift is up to +20 meV.

The exciton band FWHM also changes under acetone vapor. The FWHM shifts in the A^0 exciton emission band across the WS_2 flake show very modest effects (-10 to +10 meV), but the more positive shifts appear in areas with large energy differences and the highest sensitivity to acetone quenching. The FWHM shifts in the AA exciton emission band across the WS_2 flake exhibit an interesting pattern. In single-layer WS_2 regions with high AA exciton emission band sensitivity to acetone, the band FWHM shift is up to +60 meV. In the few-layer WS_2 region, the band FWHM shifts are slightly larger (up to +80 meV). This could arise from the topmost WS_2 layer within the few-layer region. The exciton emission band FWHM shifts in the A^- exciton band across the WS_2 flake exhibit a striking pattern. In the single-layer region, the band FWHM shifts are generally -50 to -80 meV, but there are regions with -20 meV shifts at the flake edges that also correspond to a high PL quenching sensitivity. In the immediate area surrounding the few-layer region, the FWHM shifts are the largest (up to -100 meV). This area corresponds to the region where acetone-induced PL enhancement is observed.

Figure 10 is a model to summarize the single- and few-layer WS_2 exciton PL emission behavior in the presence of acetone. Acetone causes an overall decrease in the A^0 and AA exciton band PL emission for single- and few-layer WS_2 . A decrease in PL emission was also produced in the A^- exciton band PL emission in few-layer WS_2 , but there is an overall increase in the A^- exciton band PL emission from single-layer WS_2 .

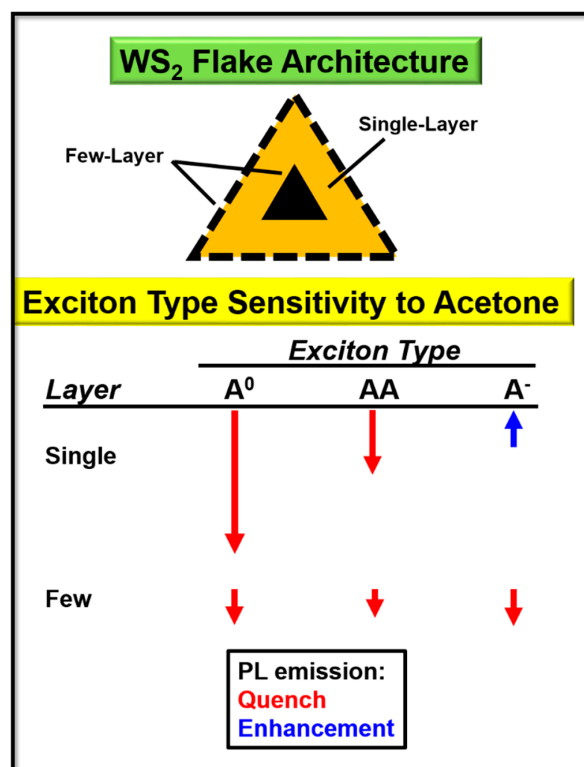


Figure 10. Model of the overall effect of acetone on exciton bands. A WS_2 flake in an air environment denoting single- and few-layer areas. The red arrows indicate a quench in PL and the blue arrow indicates an enhancement. The arrow length represents the effect magnitude.

4. Conclusions

Atomic force microscopy, Raman, and PL maps were used to determine the WS₂ layer thickness and map the A⁰, AA, and A⁻ PL emission exciton band contribution within the flake for chemical sensing assessment. Analyte vapor studies show that the PL response from the WS₂ flake is exciton-type and layer number dependent. It has been shown that the exciton amplitude, energy, and FWHM are all affected by acetone vapor. The A⁰ exciton PL emission is most strongly quenched by acetone whereas the A⁻ exciton PL emission shows a unique PL enhancement under acetone vapors. The results identify interesting strategies to generate unique, analyte-dependent responses from single- and few layer WS₂ platforms. We are currently investigating single- and few-layer WS₂ PL exciton band behavior on sapphire and SiO₂/Si substrates.

Supplementary Materials: The following are available online at <http://www.mdpi.com/1424-8220/19/8/1913/s1>, Figure S1: Initial Raman maps and layer count ratio. Figure S2: Initial Raman maps and layer count difference. Figure S3: Simplified schematic depicting WS₂ fabrication.

Author Contributions: S.M. contributed to the acquisition, analysis, and interpretation of data, and drafting the original manuscript. C.Z. contributed to the fabrication of the material. H.Z. contributed to the review and editing of the manuscript. F.V.B. contributed to the conceptualization, data interpretation, and manuscript preparation and editing.

Funding: This research was funded by the National Science Foundation, grant number CHE-1411435. Any opinions, findings, and conclusions or recommendations expressed in this material are those of the authors and do not necessarily reflect the views of the National Science Foundation.

Acknowledgments: The authors would like to thank Gary Nottingham from the UB College of Arts and Sciences Machine Shop for designing and fabricating the Teflon flow cell used in this research.

Conflicts of Interest: The authors declare no conflict of interest.

References

1. Rout, C.S.; Joshi, P.D.; Kashid, R.V.; Joag, D.S.; More, M.A.; Simbeck, A.J.; Washington, M.; Nayak, S.K.; Late, D.J. Superior Field Emission Properties of Layered WS₂-RGO Nanocomposites. *Sci. Rep.* **2013**, *3*, 1–8. [[CrossRef](#)] [[PubMed](#)]
2. Berkdemir, A.; Gutiérrez, H.R.; Botello-Méndez, A.R.; Perea-López, N.; Elías, A.L.; Chia, C.-I.; Wang, B.; Crespi, V.H.; López-Urías, F.; Charlier, J.-C.; et al. Identification of Individual and Few Layers of WS₂ Using Raman Spectroscopy. *Sci. Rep.* **2013**, *3*, 1–8. [[CrossRef](#)]
3. Lv, R.; Robinson, J.A.; Schaak, R.E.; Sun, D.; Sun, Y.; Mallouk, T.E.; Terrones, M. Transition Metal Dichalcogenides and Beyond: Synthesis, Properties, and Applications of Single- and Few-Layer Nanosheets. *Acc. Chem. Res.* **2015**, *48*, 56–64. [[CrossRef](#)]
4. Mitioglu, A.A.; Plochocka, P.; Jadczyk, J.N.; Escoffier, W.; Rikken, G.L.J.A.; Kulyuk, L.; Maude, D.K. Optical Manipulation of the Exciton Charge State in Single Layer Tungsten Disulfide. *Phys. Rev. B* **2013**, *88*, 1–5. [[CrossRef](#)]
5. Zhao, W.; Ghorannevis, Z.; Chu, L.; Toh, M.; Kloc, C.; Tan, P.-H.; Eda, G. Evolution of Electronic Structure in Atomically Thin Sheets of WS₂ and WSe₂. *ACS Nano* **2013**, *7*, 791–797. [[CrossRef](#)] [[PubMed](#)]
6. Yoffe, A.D. Layer Compounds. *Annu. Rev. Mater. Res.* **1973**, *3*, 147–170. [[CrossRef](#)]
7. Thripuranthaka, M.; Late, D.J. Temperature Dependent Phonon Shifts in Single-Layer WS₂. *ACS Appl. Mater. Interfaces* **2014**, *6*, 1158–1163.
8. Kotlyar, R.; Avci, U.E.; Cea, S.; Rios, R.; Linton, T.D.; Kuhn, K.J.; Young, I.A. Bandgap Engineering of Group IV Materials for Complementary n and p Tunneling Field Effect Transistors. *Appl. Phys. Lett.* **2013**, *102*, 1–4. [[CrossRef](#)]
9. Late, D.J.; Huang, Y.-K.; Liu, B.; Acharya, J.; Shirodkar, S.N.; Luo, J.; Yan, A.; Charles, D.; Waghmare, U.V.; Dravid, V.P.; et al. Sensing Behavior of Atomically Thin-Layered MoS₂ Transistors. *ACS Nano* **2013**, *7*, 4879–4891. [[CrossRef](#)]
10. Perkins, F.K.; Friedman, A.L.; Cobas, E.; Campbell, P.M.; Jernigan, G.G.; Jonker, B.T. Chemical Vapor Sensing with Monolayer MoS₂. *Nano Lett.* **2013**, *13*, 668–673. [[CrossRef](#)]

11. Huo, N.; Yang, S.; Wei, Z.; Li, S.S.; Xia, J.B.; Li, J. Photoresponsive and Gas Sensing Field-Effect Transistors Based on Multilayer WS₂ Nanoflakes. *Sci. Rep.* **2014**, *4*, 1–9. [[CrossRef](#)]
12. Perrozzi, F.; Emamjomeh, S.M.; Paolucci, V.; Taglieri, G.; Ottaviano, L.; Cantalini, C. Thermal Stability of WS₂ Flakes and Gas Sensing Properties of WS₂/WO₃ Composite to H₂, NH₃, and NO₂. *Sens. Actuators B Chem.* **2017**, *243*, 812–822. [[CrossRef](#)]
13. Bui, V.Q.; Pham, T.T.; Le, D.A.; Thi, C.M.; Le, H.M. A First-Principles Investigation of Various Gas (CO, H₂O, NO, and O₂) Absorptions on a WS₂ Monolayer: Stability and Electronic Properties. *J. Phys. Condens. Matter* **2015**, *27*, 1–11. [[CrossRef](#)]
14. Donarelli, M.; Ottaviano, L. 2D Materials for Gas Sensing Applications: A Review on Graphene Oxide, MoS₂, WS₂ and Phosphorene. *Sensors* **2018**, *18*, 3638. [[CrossRef](#)]
15. Cho, B.; Hahm, M.G.; Choi, M.; Yoon, J.; Kim, A.R.; Lee, Y.J.; Park, S.G.; Kwon, J.D.; Kim, C.S.; Song, M.; et al. Charge-Transfer-Based Gas Sensing Using Atomic-Layer MoS₂. *Sci. Rep.* **2015**, *5*, 1–6. [[CrossRef](#)]
16. Gutierrez, H.R.; Perea-Lopez, N.; Elias, A.L.; Berkdemir, A.; Wang, B.; Lv, R.; Lopez-Urias, F.; Crespi, V.H.; Terrones, H.; Terrones, M. Extraordinary Room-Temperature Photoluminescence in Triangular WS₂ Monolayers. *Nano Lett.* **2013**, *13*, 3447–3454. [[CrossRef](#)]
17. Eda, G.; Yamaguchi, H.; Voiry, D.; Fujita, T.; Chen, M.; Chhowalla, M. Photoluminescence from Chemically Exfoliated MoS₂. *Nano Lett.* **2011**, *11*, 5111–5116. [[CrossRef](#)] [[PubMed](#)]
18. Kim, M.S.; Yun, S.J.; Lee, Y.; Seo, C.; Han, G.H.; Kim, K.K.; Lee, Y.H.; Kim, J. Biexciton Emission from Edges and Grain Boundaries of Triangular WS₂ Monolayers. *ACS Nano* **2016**, *10*, 2399–2405. [[CrossRef](#)]
19. Taheri, P.; Wang, J.; Xing, H.; Destino, J.F.; Arik, M.M.; Zhao, C.; Kang, K.; Blizzard, B.; Zhang, L.; Zhao, P.; et al. Growth Mechanism of Largescale MoS₂ Monolayer by Sulfurization of MoO₃ Film. *Mater. Res. Express* **2016**, *3*, 1–10. [[CrossRef](#)]
20. Cong, C.; Shang, J.; Wu, X.; Cao, B.; Peimyoo, N.; Qiu, C.; Sun, L.; Yu, T. Synthesis and Optical Properties of Large-Area Single-Crystalline 2D Semiconductor WS₂ Monolayer from Chemical Vapor Deposition. *Adv. Opt. Mater.* **2014**, *2*, 131–136. [[CrossRef](#)]
21. Hegner, M.; Wagner, P.; Semenza, G. Ultralarge Atomically Flat Template-Stripped Au Surfaces for Scanning Probe Microscopy. *Surf. Sci.* **1993**, *291*, 39–46. [[CrossRef](#)]
22. Gurarlan, A.; Yu, Y.; Su, L.; Yu, Y.; Suarez, F.; Yao, S.; Zhu, Y.; Ozturk, M.; Zhang, Y.; Cao, L. Surface-Energy-Assisted Perfect Transfer of Centimeter-Scale Monolayer and Few-Layer MoS₂ Films onto Arbitrary Substrates. *ACS Nano* **2014**, *8*, 11522–11528. [[CrossRef](#)] [[PubMed](#)]
23. Eaton, P.; West, P. AFM Modes. In *Atomic Force Microscopy*; Oxford University Press: Oxford, UK, 2010; pp. 69–71.
24. Zhao, W.; Ribeiro, R.M.; Toh, M.; Carvalho, A.; Kloc, C.; Castro Neto, A.H.; Eda, G. Origin of Indirect Optical Transitions in Few-Layer MoS₂, WS₂, and WSe₂. *Nano Lett.* **2013**, *13*, 5627–5634. [[CrossRef](#)] [[PubMed](#)]
25. Lakowicz, J.R. Quenching of Fluorescence. In *Principles of Fluorescence Spectroscopy*; Kluwer Academic/Plenum Publishers: New York, NY, USA, 2013; pp. 278–281.
26. Bukowski, R.M.; Ciriminna, R.; Pagliaro, M.; Bright, F.V. High-Performance Quenchometric Oxygen Sensors Based on Fluorinated Xerogels Doped with [Ru(dpp)₃]²⁺. *Anal. Chem.* **2005**, *77*, 2670–2672. [[CrossRef](#)] [[PubMed](#)]
27. Ko, K.Y.; Song, J.-G.; Kim, Y.; Choi, T.; Shin, S.; Lee, C.W.; Lee, K.; Koo, J.; Lee, H.; Kim, J.; et al. Improvement of Gas-Sensing Performance of Large-Area Tungsten Disulfide Nanosheets by Surface Functionalization. *ACS Nano* **2016**, *10*, 9287–9296. [[CrossRef](#)]
28. Friedman, A.L.; Perkins, F.K.; Cobas, E.; Jernigan, G.G.; Campbell, P.M.; Hanbicki, A.T.; Jonker, B.T. Chemical Vapor Sensing of Two-Dimensional MoS₂ Field Effect Transistor Devices. *Solid State Electron.* **2014**, *101*, 2–7. [[CrossRef](#)]

